# Crystal Structures of *Mycobacterium tuberculosis* CysQ, with Substrate and Products Bound

Anna I. Erickson,[§] Reta D. Sarsam,[‡] and Andrew J. Fisher[*,‡,†]

[†]Department of Chemistry, [‡]Department of Molecular and Cellular Biology, and [§]Graduate Program in Biochemistry and Molecular, Cellular and Developmental Biology, University of California, One Shields Avenue, Davis, California 95616, United States
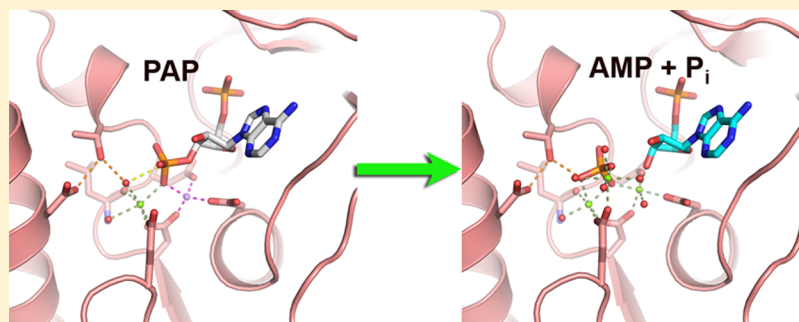
ABSTRACT: In many organisms, 3′-phosphoadenosine 5′-phosphate (PAP) is a product of two reactions in the sulfur activation pathway. The sulfurylation of biomolecules, catalyzed by sulfotransferases, uses 3′-phosphoadenosine 5′-phosphosulfate (PAPS) as a sulfate donor, producing the sulfated biomolecule and PAP product. Additionally, the first step in sulfate reduction for many bacteria and fungi reduces the sulfate moiety of PAPS, producing PAP and sulfite, which is subsequently reduced to sulfide. PAP is removed by the phosphatase activity of CysQ, a 3′,5′-bisphosphate nucleotidase, yielding AMP and phosphate. Because excess PAP alters the equilibrium of the sulfur pathway and inhibits sulfotransferases, PAP concentrations can affect the levels of sulfur-containing metabolites. Therefore, CysQ, a divalent cation metal-dependent phosphatase, is a major regulator of this pathway. CysQ (Rv2131c) from *Mycobacterium tuberculosis* (*Mtb*) was successfully expressed, purified, and crystallized in a variety of ligand-bound states. Here we report six crystal structures of *Mtb* CysQ, including a ligand-free structure, a lithium-inhibited state with substrate PAP bound, and a product-bound complex with AMP, phosphate, and three Mg^{2+} ions bound. Comparison of these structures together with homologues of the superfamily has provided insight into substrate specificity, metal coordination, and catalytic mechanism.

Tuberculosis (TB), caused by *Mycobacterium tuberculosis* (*Mtb*) infection, kills approximately 1.5 million people each year. The World Health Organization (WHO) estimates 9.0 million new cases of TB occurred in 2013, of which approximately 3.5% are categorized as multidrug-resistant TB (MDR-TB).[1] Multidrug-resistant strains are resistant to isoniazid and rifampin, the two most commonly used first-line drugs. Extensively drug-resistant TB (XDR-TB) is resistant to the same drug treatments as MDR as well as fluoroquinolone derivatives and at least one of the injectable second-line drugs. Drug-resistant strains of *Mtb* present a global threat and necessitate the development of novel antibiotics for treating these new drug-resistant strains.[1,2] Recent research has found *Mtb* genes involved in sulfur metabolism are upregulated and support the persistent stage of infection;[3−10] consequently, these sulfur-related gene products may present novel targets for drug discovery.[11−13]

The sulfur activation pathway converts relatively inert sulfate into more reactive sulfur-containing metabolites found in cells. The first step of sulfate activation is catalyzed by ATP sulfurylase, which in *Mycobacterium* consists of the CysD−CysNC heterodimeric G-protein that couples GTP hydrolysis to adenylyl transfer to sulfate, generating adenosine 5′-phosphosulfate (APS) (Figure 1). APS can be either directly reduced to sulfite by APS reductase (CysH) or phosphorylated by APS kinase to form 3′-phosphoadenosine 5′-phosphosulfate (PAPS), the universal sulfate donor.[14,15] In *Mycobacterium*, this phosphorylation step is conducted by the APS kinase domain (CysC), which is found at the C-terminal end of the CysNC gene product.[8] Sulfotransferases use PAPS as a sulfate donor to produce a variety of sulfate-containing metabolites[16] and sulfated proteins.[17] The product molecule, 3′-phosphoadenosine 5′-monophosphate (PAP), of the sulfur transfer reaction is a competitive inhibitor of sulfotransferases.[12,18,19] Accumulation of PAP in the cell has been shown to disrupt the sulfur activation pathway in bacteria,[19,20] yeast,[21] and mammals[22] and can inhibit exoribonucleases.[23] In *Mtb*, a CysQ knockout resulted in reduced levels of the sulfated glycolipid Sulfolipid-1 and attenuation of cell growth.[19]
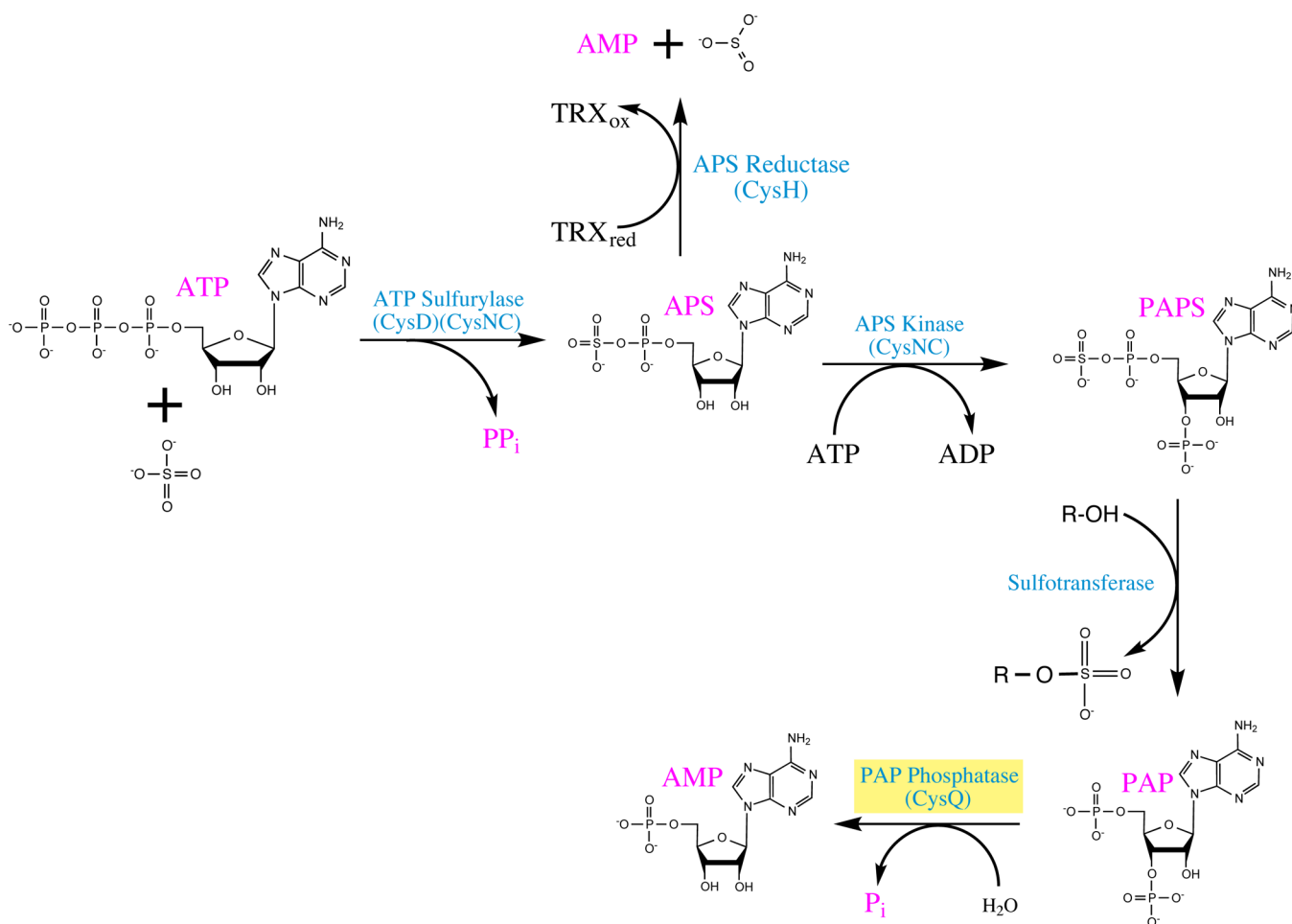
Figure 1. Sulfur activation pathway of *Mtb*. Gene product names are listed in parentheses. The structures reported here are different bound states of CysQ, highlighted in yellow.

PAP is also generated in many organisms that reduce PAPS instead of APS in the sulfate reduction step. In most fungi and bacteria (not *Mycobacterium*), PAPS is the substrate of the first sulfur reduction step instead of APS. PAPS is reduced by PAPS reductase to generate PAP and sulfite. However, the mechanisms of PAPS reductase and APS reductase are very similar.[24]

PAP is broken down by CysQ (Rv2131c) (EC 3.1.3.7), a 3′-phosphoadenosine 5′-phosphatase, converting PAP to AMP and inorganic phosphate (Figure 1). CysQ is part of the larger FIG superfamily of phosphatases that dephosphorylates a monosaccharide-containing substrate. The FIG superfamily is comprised of family members: fructose-1,6-bisphosphatase (FBPase), inositol-monophosphatases (IMPase)/polyphosphatases (IPPase), and the glpX-encoded variant of FBPase (Class II). Many members of this superfamily display promiscuous phosphatase activity toward various monosaccharide-containing substrates but are usually more efficient in one type, which identifies their subfamily class.[25−30] For example, *Mtb* CysQ can dephosphorylate *myo*-inositol 1-phosphate (IMP), fructose 1,6-bisphosphate (FBP), and 3′-phosphoadenosine 5′-monophosphate (PAP), but the catalytic efficiency is 1700- and 15000-fold greater for PAP over FBP and IMP, respectively.[31]

The FIG superfamily enzymes have demonstrated a dependence on divalent metal ions and are most active with magnesium (Mg^{2+})[31,32] with three Mg^{2+} ions binding in the active site to form a productive enzyme.[29,33,34] The superfamily also displays

sensitivity to monovalent metals, and members are most strongly inhibited by lithium (Li^+).[31,35,36] The Li^+ ion displaces Mg^{2+} ion, specifically the Mg^{2+} ion at metal site 2, and is thought to stabilize the phosphate-bound product.[37−39] The inhibition by lithium suggests this superfamily of enzymes is the target of lithium therapy in manic-depressive illness.[36,40−43]

Members of the FIG enzyme superfamily display low levels of sequence identity but retain a common fold and a similar active site. Numerous structures of IMPase and FBPase subfamilies from many organisms have been determined, but only three structures of CysQ phosphatase have been determined from the organisms: yeast (Hal2p),[39,44] *Entamoeba histolytica*,[27] and recently human [unpublished, Protein Data Bank (PDB) entry 2WEF]. The yeast Hal2p structures were determined with products AMP, phosphate, and three Mg^{2+} ions bound, and in a substrate PAP-bound inhibited state with Ca^{2+} bound in metal site 1 and Mg^{2+} bound in metal site 2.[44] Another report by the same group presents a structure with AMP and phosphate along with Li^+ ion bound to metal site 2 with Mg^{2+} binding to sites 1 and 3.[39] Because the Li^+ ion possesses only two electrons and is difficult to observe by X-ray crystallography, a lithium ion was inferred to bind to metal site 2.[39] Two structures of CysQ from *E. histolytica* were determined, one with AMP, a Mg^{2+} at site 1, and Na^+ at site 2 and a ligand-free structure with a Mg^{2+} bound at site 1.[27] Finally, the human CysQ structure was determined with products AMP, phosphate, and three Mg^{2+} ions bound. Here we present six crystal structures of CysQ from *Mtb* with

Table 1. Data Processing and Refinement Statistics

	ligand-free	heavy metal	PAP + Mg^{2+} + Li$^+$	AMP + P$_i$ + 3Mg^{2+}	AMP + P$_i$ + 2Mg^{2+}	PO$_4^{2-}$ + 2Mg^{2+}	PO$_4^{2-}$ + 2Ca^{2+}
PDB entry	5DJF		5DJG	5DJH	5DJI	5DJJ	5DJK
wavelength (Å)	1.12709	1.12709	1.12709	1.12709	1.12709	1.12709	1.12709
space group	$P2_12_12_1$	$P2_12_12_1$	$P2_12_12_1$	$P2_12_12_1$	$P2_12_12_1$	$P2_12_12_1$	$P2_12_12_1$
unit cell parameters (Å)	$a = 40.32$, $b = 57.9$, $c = 101.68$	$a = 40.6$, $b = 58.2$, $c = 102.2$	$a = 40.67$, $b = 58.06$, $c = 101.22$	$a = 40.64$, $b = 58.14$, $c = 101.2$	$a = 40.64$, $b = 58.2$, $c = 101.51$	$a = 40.05$, $b = 57.83$, $c = 101.64$	$a = 40.26$, $b = 58.23$, $c = 101.42$
resolution range (Å)	38.2–1.7 (1.74–1.70)	38.4–2.05 (2.10–2.05)	38.15–1.95 (2.00–1.95)	38.17–1.45 (1.47–1.45)	38.25–1.66 (1.70–1.66)	32.93–1.50 (1.52–1.50)	31.53–1.8 (1.84–1.8)
no. of observed reflections	83741 (4351)	55564 (4131)	58666 (1102)	151459 (10757)	52795 (4459)	134589 (9274)	80543 (5731)
no. of unique reflections	26208 (1807)	28462 (2135)	17281 (2033)	42861 (2623)	28723 (2,021)	38082 (2427)	22686 (2472)
completeness (%)	97.3 (92.7)	96.7 (97.0)	95.5 (84.1)	99.2 (97.36)	98.1 (84.0)	93.6 (88.0)	99.3 (96.9)
$I/\sigma(I)$	13.46 (2.60)	12.49 (4.40)	14.44 (4.43)	23.87 (3.47)	38.81 (9.17)	20.44 (3.12)	16.89 (2.87)
R_{merge} ^{a} (%)	6.1 (40.1)	5.1 (19.2)	7.1 (26.5)	3.3 (38.7)	2.1 (9.8)	3.5 (39.8)	5.3 (44.6)
$CC_{1/2}$	99.7 (78.1)	99.7 (90.8)	99.5 (89.9)	99.9 (84.7)	100.0 (98.2)	99.9 (82.4)	99.9 (83.3)
no. of monomers per asymmetric unit	1	1	1	1	1	1	1
Matthews coefficient (Å^3/Da)	1.95	2.16	2.13	2.13	2.14	2.10	2.12
solvent content (%)	37	43	42	42	43	42	42
Refinement							
no. of reflections ($F > 0$)	26208		17281	42862	28723	38026	22686
R_{factor} ^{b} (%)	16.46		15.80	14.87	14.23	15.62	15.51
R_{free} ^{b} (%)	19.90		18.58	16.87	16.84	17.55	18.96
rmsd for bond lengths (Å)	0.006		0.007	0.006	0.007	0.010	0.007
rmsd for bond angles (deg)	1.102		1.145	1.173	1.129	1.332	1.065
Ramachandran plot statistics^c							
favored (%)	96.98		97.99	97.62	97.21	98.07	97.60
allowed (%)	2.64		1.61	2.38	2.39	1.16	2.00
outliers (%)	0.38		0.40	0.00	0.40	0.77	0.40
no. of atoms (B factor)							
protein	2028 (20.6 Å^2)		1951 (15.8 Å^2)	1962 (20.2 Å^2)	1958 (19.3 Å^2)	1990 (23.3 Å^2)	1911 (25.2 Å^2)
ligands with metal	1 (27.2 Å^2)		29 (16.5 Å^2)	31 (14.1 Å^2)	30 (15.5 Å^2)	7 (14.7 Å^2)	7 (19.6 Å^2)
solvent	300 (33.9 Å^2)		273 (26.4 Å^2)	269 (32.0 Å^2)	295 (31.3 Å^2)	241 (33.4 Å^2)	220 (34.6 Å^2)

$^a R_{merge} = \sum_h \sum_i |I_{hi} - I_h| / \sum_h \sum_i I_{hi}$, where I_h is the mean of I_{hi} observations of reflection h. Numbers in parentheses represent data for the highest-resolution shell. $^b R_{factor}$ and $R_{free} = \sum ||F_{obs}| - |F_{calc}|| / \sum |F_{obs}| \times 100$ for 95% of the recorded data (R_{factor}) or 5% of the data (R_{free}). ^{c}Ramachandran plot statistics from MolProbity.[60]

different metals, substrates, and products bound. Three significant structures include (1) a ligand-free structure, (2) a Li$^+$-inhibited structure with substrate PAP bound, a Mg^{2+} ion bound at metal site 1, and Li$^+$ bound at metal site 2, and (3) a structure with products of AMP bound, phosphate, with all three Mg^{2+} binding sites occupied.

■ MATERIALS AND METHODS

Cloning, Overexpression, and Purification. The *Mtb cysQ* gene, *Rv2131c*, was cloned, overexpressed, and purified as described previously.[45] The pET 28b(+) *cysQ* construct was overexpressed in *Escherichia coli* BL21(DE3). When the cells reached a density of OD$_{600}$ ≥ 0.5, protein production was induced with 150 μM isopropyl β-D-1-thiogalactopyranoside (IPTG) for 20 h at 18 °C with 220 rpm shaking. Cells were collected by centrifugation (15 min at 5000g) and lysed by being passed through a microfluidizer in lysis buffer [30 mM imidazole, 50 mM NaH$_2$PO$_4$ (pH 8), and 800 mM NaCl]. The lysate was cleared by centrifugation at 30000g for 40 min at 4 °C.

The cell lysate was loaded on pre-equilibrated Ni^{2+}-NTA resin (Sigma, St. Louis, MO). The column was washed with 100 column volumes of lysis buffer and eluted with a linear gradient from 30 to 250 mM imidazole using elution buffer [250 mM imidazole, 300 mM NaCl, and 50 mM NaH$_2$PO$_4$ (pH 8)]. The extensive column washing prior to elution helped remove nonspecific proteins binding to the column. Protein fractions were identified by absorbance at 280 nm, and purity was analyzed by sodium dodecyl sulfate–polyacrylamide gel electrophoresis stained with Coomassie Blue. Pure CysQ fractions were pooled and dialyzed overnight against 400 mM NaCl, 20 mM Tris (pH 8), 1 mM DTT, and 5% glycerol. The typical total protein volume was 20 mL, which was dialyzed against 2 L of dialysis buffer. CysQ was concentrated in an Amicon 10K molecular weight cutoff spin concentrator (Millipore) and buffer exchanged three times with 20 mM Tris (pH 8), 100 mM NaCl, 1 mM DTT, 5% glycerol, and 1 mM AMP. The total volume of exchange buffer was 20 mL divided into three centrifuge spins. The final protein concentration was 10 mg/mL and used directly in sitting drop vapor-diffusion crystallization trays.

Crystallization and Data Collection. Initial crystallization conditions were found using the commercially available Microlytic crystallization screens MCSG 1 and MCSG 2. Twenty-four-well plates were used to further optimize crystallization hits observed in the MCSG screens. Crystals grew at room temperature (21 °C) in droplets of 1 μL of 10 mg/mL CysQ and 1 μL of a reservoir solution forming over 1−5 days.

The ligand-free enzyme (PDB entry 5DJF) grew in 24% PEG 1500 and 20% glycerol; the crystal was flash-cooled in its mother liquor. The calcium- and phosphate-bound structure (PDB entry 5DJK) was grown in 0.05 M CaCl$_2$, 0.1 M Bis-Tris-HCl (pH 6.5), and 30% PEG MME 550. The crystal was flash-cooled in its mother liquor. The magnesium- and phosphate-bound structure (PDB entry 5DJJ) was grown in 0.1 M Mg acetate, 0.1 M Bis-Tris-HCl (pH 6.5), and 35% PEG MME 550 and flash-cooled in its mother liquor. For both the Ca^{2+} and Mg^{2+} structures, phosphate was not included in the crystallization conditions, but in both cases, clear electron density revealed phosphate binding along with two divalent metal binding ions in metal sites 1 and 2. The phosphate is likely a contaminant in the crystallization buffer carried over by the protein from the purification buffers. The possibility that trace contamination of

phosphate might be present in the crystallization buffer before the addition of protein cannot be ruled out. The AMP-, P$_i$-, and Mg^{2+}-bound structures were crystals grown in 0.1 M Mg acetate, 0.1 M Bis-Tris-HCl (pH 6.5), and 35% PEG MME 550 and soaked for 20 min in mother liquor supplemented with 3 mM AMP before being flash-cooled in the mother liquor. X-ray diffraction data were collected from multiple crystals and upon analysis revealed that one structure contained AMP, PO$_4^{2-}$, and two Mg^{2+} ions (metal sites 1 and 2) (PDB entry 5DJI) and another crystal contained AMP, PO$_4^{2-}$, and all three Mg^{2+} ions bound (PDB entry 5DJH). Again, no phosphate was included in the crystallization condition but likely came from buffer contaminant or AMP breakdown. The PAP-bound structure (PDB entry 5DJG) was cocrystallized in 0.2 M LiCl$_2$, 25% PEG 8000, and 1 mM PAP. The crystal was transferred to a cryo-solution before being flash-cooled (0.2 M LiCl$_2$, 25% PEG 8000, and 20% ethylene glycol).

All diffraction data were collected at the Stanford Synchrotron Radiation Lightsource (SSRL), beamline 7-1. All data sets were collected using the fine phi technique with an oscillation angle of 0.3°. Data were processed with XDS and scaled with XSCALE.[46,47] CysQ crystallized in the orthorhombic point group 222 with the following unit cell parameters: a = 40.0−40.6 Å, b = 57.8−58.2 Å, and c = 101.2−102.2 Å. Inspection of the systematic absences of each data set suggests space group P2$_1$2$_1$2$_1$. Matthews coefficients were calculated to be 1.95−2.16 Å^3/Da, resulting in a solvent content of 37−43% assuming one monomer per asymmetric unit.[48] See Table 1 for individual statistics for each data set, including data processing and structure refinement statistics.

Structure Solutions and Refinements. Attempts to determine the initial structure by molecular replacement were unsuccessful using the closest known structural homologues. Therefore, SIRAS (Single Isomorphous Replacement with Anomalous Scattering) phasing information was collected from a ligand-free crystal grown in 0.2 M calcium acetate, 0.1 M MES-NaOH (pH 6.0), and 20% (w/v) PEG 8000 that was soaked overnight in mother liquor supplemented with a heavy atom cocktail: 1 mM uranyl acetate, 1 mM p-chloromercury benzoic acid sulfonate (PCMBS), and 1 mM KAu(CN)$_2$. Before being flash-cooled, the crystal was transferred to a cryo-solution [0.2 M Ca acetate, 0.1 M MES-NaOH (pH 6.0), 20% (w/v) PEG 8000, and 20% glycerol]. Phases were calculated using SIRAS protocols in SHELX C/D/E[49] to search for mercury atoms. Although any of the heavy atoms (U, Hg, and Au) could bind to the protein, the software would adjust for ambiguous heavy atoms by refining occupancy and temperature factors of the heavy atom positions. The SIRAS structure revealed heavy atoms binding to soft ligands that were not cysteine residues, suggesting the gold atoms bound to the structure. PHENIX[50] was used to build the initial preliminary model, which was completed manually using COOT.[51] Subsequent structures were determined by molecular replacement using PHASER[52] as part of the CCP4 software package.[53] All structures were refined by PHENIX.[50] Final refinement statistics are listed in Table 1.

■ RESULTS AND DISCUSSION

Overall Structure of CysQ. Like other members of the FIG superfamily, the protein structure contains two topological domains, an N-terminal domain that is a member of the α + β class and the C-terminal domain of the α/β class. The two domains pack together to form a five-layered interleaved structure of alternating α-helices and β-sheets forming an

α−β−α−β−α structure (Figure 2). Each helix layer consists of two α-helices, and the two β-sheets are both five-stranded mixed
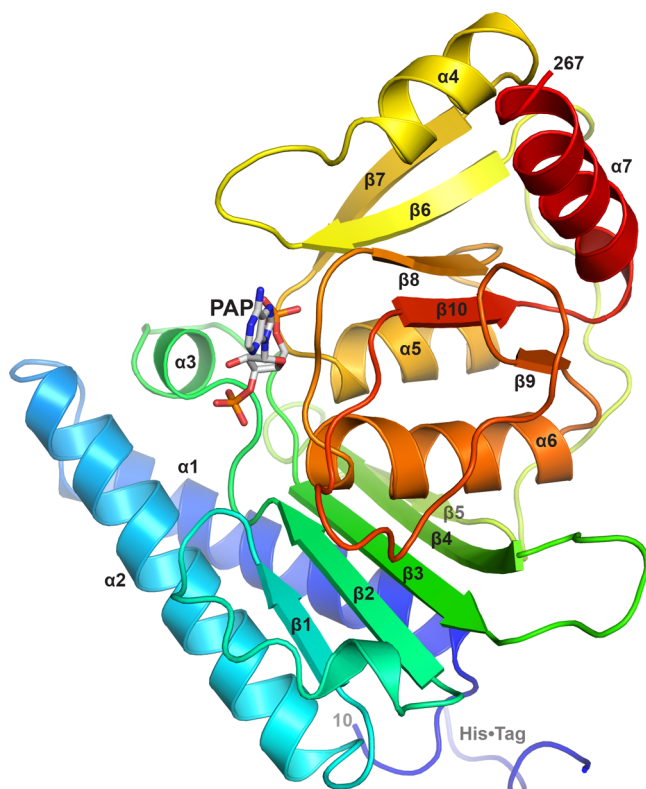

Figure 2. Overall structure of *Mtb* CysQ with PAP shown to identify the active site. The ribbon color starts at the N-terminus with blue and changes according to the visible spectrum ending with red at the C-terminus. The N-terminal His tag is labeled; however, electron density was not observed for residues −2 to 10, so they are not included in the final structure. Figures 2−4 and 6 were generated with PyMol (www.pymol.org).

β-sheets. The long loop that connects the two topological domains together, between β5 and β6 (Figure 2), is disordered for residues 147−152 for structures that have nucleotide bound to the active site. This is unexpected because this loop is >20 Å away on the backside of the enzyme, with respect to the active site. It is unknown if nucleotide binding affects this loop movement or conformation.

Six structures of *Mtb* CysQ were determined with different combinations of metal ions, substrates, and products bound in the active site (Table 1). For all structures, part of the N-terminal His tag is visible because it helps mediate crystal packing contacts, but the loop between the His tag and residue 10 is disordered in all structures. The first structure was determined in the absence of any ligands or divalent cations; however, a potential Na^+ ion bound near metal site 1, suggested by the PHENIX metal placement algorithm, which identifies metals on the basis of electron density, ligand geometry, and distances. This ion is pentacoordinated with an average ligand distance of 2.6 Å. Two *Mtb* CysQ structures were determined with only the divalent cations (Ca^{2+} or Mg^{2+}) added to the crystallization conditions, but both crystallized with phosphate and two ions in the active site (metal sites 1 and 2 occupied). The phosphate is likely coming from a minor contamination in buffer or salts used to make the buffer. This suggests that for CysQ, divalent cations may not be able to bind the active site

without a substrate or phosphate product. This is in contrast to yeast CysQ (Hal2p), which was able to crystallize with three Zn^{2+} ions binding to the active site with no phosphate moieties (PDB entry 1K9Z), Many of the IMPase structures also have Mg^{2+} ions binding without phosphate.[34,54,55] Next, a *Mtb* CysQ structure was determined with PAP binding to the active site. Crystals were grown in buffer containing 200 mM lithium chloride, which strongly inhibits the enzyme. Finally, two structures were determined with AMP, PO_4^{2-}, and Mg^{2+} ions in the active site; one structure contained two Mg^{2+} ions, and the other structure contained all three Mg^{2+} ions. For the majority of this article, we will focus discussions and comparisons on three structures: ligand-free form, PAP substrate-bound complex, and AMP- and P_i product-bound complex.

Conformational Changes upon Ligand Binding. The overall root-mean-square deviation (rmsd) between the ligand-free and nucleotide-bound structures is 0.77 and 0.76 Å for the PAP- and AMP-bound structures, respectively, based on 237 equivalent α-carbons. Comparing the ligand-free structure to structures with bound nucleotide in the active site revealed a closure of a loop over the nucleotide base. This loop, which is the loop between β6 and α4, contains an arginine residue (Arg165) where the guanidino group moves ∼11 Å from a solvent-exposed position down to π-stack against the adenine base of both PAP and AMP (Figure 3). The nucleotide is
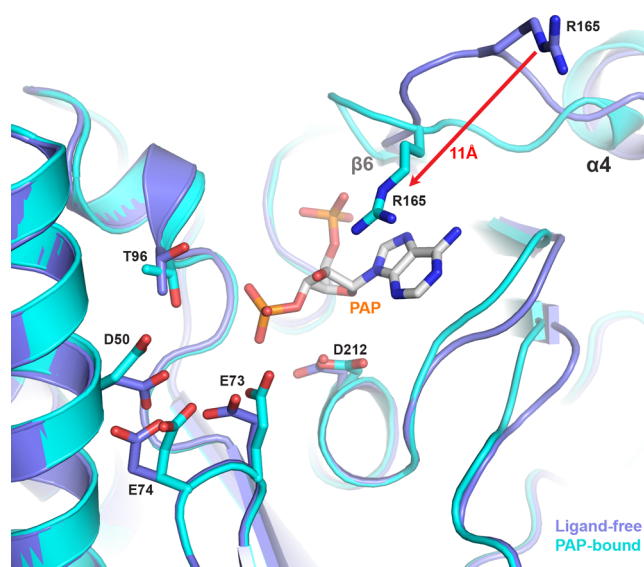
Figure 3. Conformational changes upon binding nucleotide. Shown is the superposition of the ligand-free structure (blue) onto the PAP-bound structure (cyan). The guanidino group Arg165, in the β6−α4 loop, swings down ∼11 Å to form a π-stack with the adenine. Other structural changes in identified residues also move to bind metals.

required for this loop movement because the phosphate-bound structures, with divalent metal ions, do not exhibit any changes compared to the ligand-free structure. Ser162, at the start of the loop, hydrogen bonds to the 5′-phosphate and may help trigger the closure of the loop. Two sequential proline residues (Pro166 and Pro167) following Arg165 may help maintain a rigid switch on this loop movement. Ser162 is highly conserved in the CysQ family, but Arg165 is not. The equivalent residue is a histidine residue in many CysQ sequences, including the yeast Hal2p, *E. histolytica* CysQ, and human CysQ where the imidazole ring was found to stack against the adenine ring.[27,39]
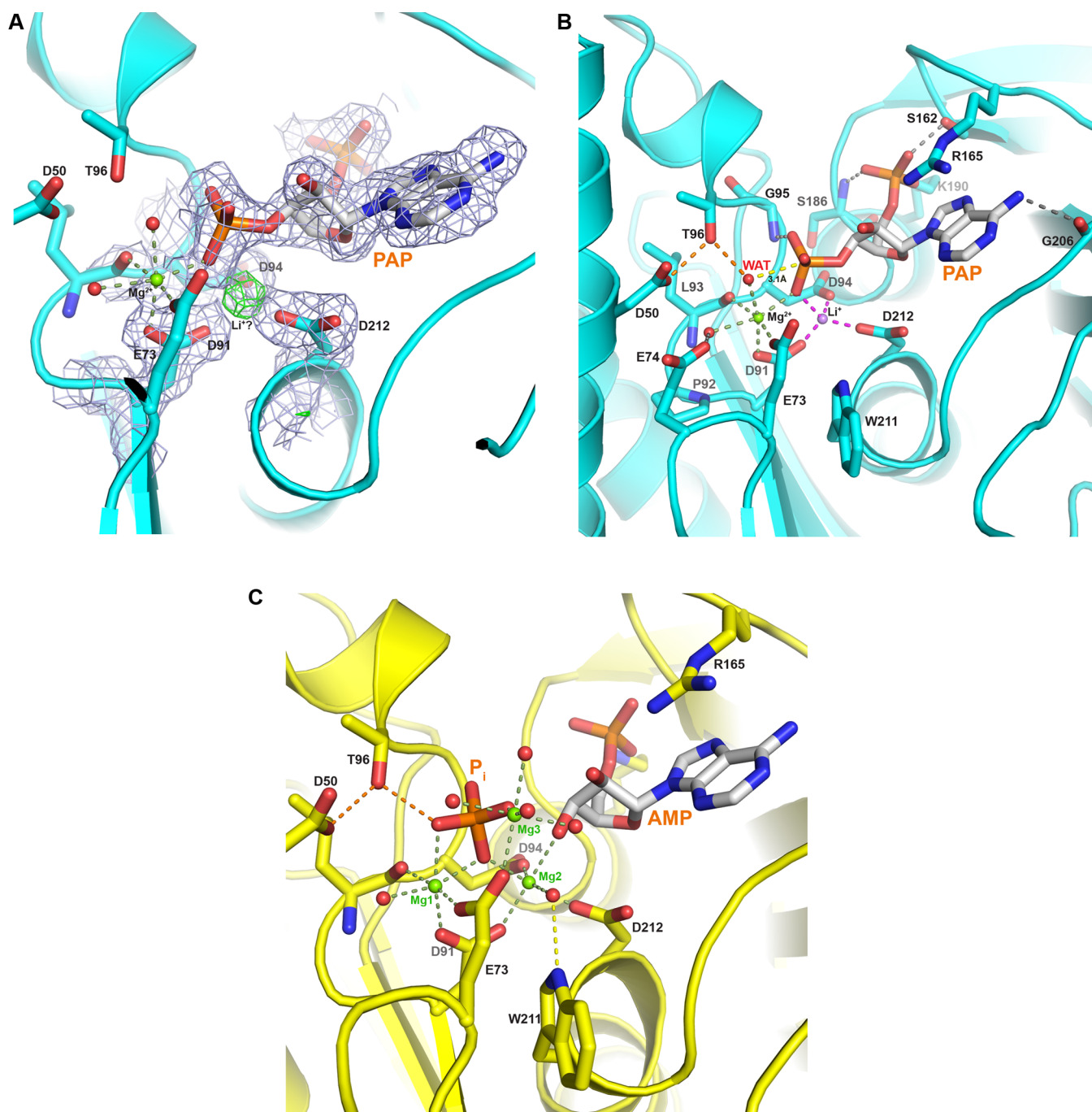
Figure 4. (A) Electron density of *Mtb* CysQ bound to PAP. The $2F_o - F_c$ electron density (light blue) is contoured at 1σ and illustrates the represented density for the PAP substrate, and residues Asp91, Aps94, and Asp212 that may bind a Li^+ ion. Shown in green is the $F_o - F_c$ difference density contoured at 3σ, illustrating the positive density at metal site 2. This site may contain a lithium ion. (B) Active site structure of the PAP-bound *Mtb* CysQ structure. Shown as sticks with white-colored carbons is the PAP substrate. Metal site 1 is occupied by Mg^{2+} with octahedral coordination shown as green dashed lines. Metal site 2 is likely occupied by Li^+, which is tetrahedrally coordinated (magenta dashed lines). Hydrogen bonds between the PAP substrate and protein are shown as gray dashed lines. The water ligand of Mg^{2+} ion that is labeled "WAT" is 3.1 Å from the phosphorus atom (yellow dashed line) and serves as the nucleophile during catalysis. (C) Active site structure of the AMP- and P_i-bound *Mtb* CysQ structure. AMP is shown with white-colored carbon atoms. Mg^{2+} ions occupy all three metal sites, with their octahedral geometry drawn as green dashed lines. Mg1−Mg3 represent Mg^{2+} ions binding to metal sites 1−3, respectively.

In addition to the $\beta6-\alpha4$ loop movement upon binding nucleotide, the side chains of residues Glu73, Glu74, and Asp212 also shift to ligate the divalent metals. Finally, the side chains of residues Asp50 and Thr96, which are implicated in catalysis, also move upon binding metals and nucleotides

(Figure 3). These ligand-induced movements that occur within the active site properly orient residues for catalysis.

Active Site. *PAP-Bound Structure.* The structures of *Mtb* CysQ with bound substrate (PAP) and products (AMP and P_i) with Mg^{2+} ions permit a more complete structural analysis of the enzyme's active site. As mentioned above, the $\beta6-\alpha4$ loop
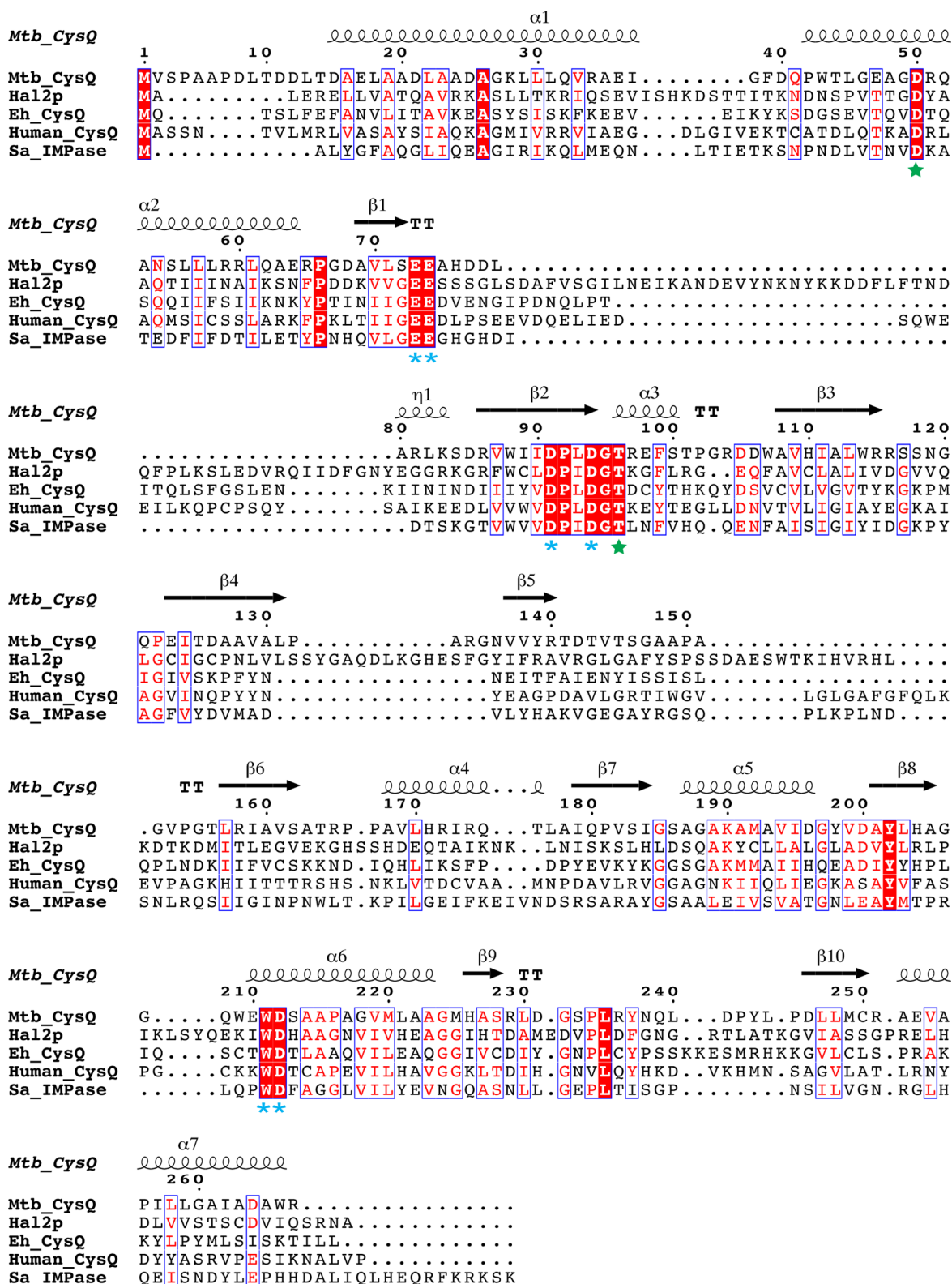
Figure 5. Protein sequence alignment of forms of CysQ from various organisms. Secondary structure elements, as observed in the *Mtb* CysQ structure, are drawn above the sequence. Residues involved in coordinating metal ions either directly or indirectly are indicated with a blue-colored asterisk. A green star marks residues implicated in catalysis. For the sequences, Hal2p is yeast CysQ, Eh_CysQ is from *E. histolytica*, the human sequence is from PDB entry 2WEF [which is annotated as 3′(2′), 5′-Bisphosphate Nucleotidase 1], and Sa_IMPase is IMPase from *Staphylococcus aureus* (numbers reflect the *Mtb* CysQ sequence). Figure was generated using the ESPript 3.0 server.[61]

containing Arg165 moves to interact with the nucleotide base together with many residues implicated in divalent metal binding.

To trap the enzyme with substrate PAP bound, we crystallized CysQ in the presence of PAP and high concentrations of lithium ions (200 mM), which inhibits *Mtb* CysQ with an IC$_{50}$ of 0.5

mM[31] and is a general inhibitor of other members of the FIG superfamily.[36] The resulting structure clearly revealed the substrate PAP binding to the active site along with one Mg^{2+}, which occupied cation binding site 1 (Figure 4A). Of the three Mg^{2+} binding sites, site 1 has the highest affinity, followed by site 2, and site 3 with the lowest affinity.[56]

Metal site 1 clearly shows electron density for a Mg^{2+} ion that is octahedrally coordinated by Asp91 Oδ1 (Oδ2 coordinates to Li$^+$), a phosphate oxygen (which also coordinates Li$^+$), Glu73 Oε1, the carbonyl oxygen of Leu93, and two water molecules. One water ligand is hydrogen-bonded to conserved Glu74. The other water ligand, which hydrogen bonds to conserved Thr96, is 3.1 Å from the phosphorus atom of the PAP 3′-phosphate and is in ideal position for a nucleophilic attack (Figure 4B).

Intriguing electron density features appeared near metal site 2 upon the final stages of refinement of the lithium-inhibited PAP bound structure. While no $2F_o - F_c$ electron density revealed a metal binding at site 2, a positive peak of $F_o - F_c$ difference density does appear at metal site 2 (Figure 4A). The absence of $2F_o - F_c$ electron density at metal sites 2 and 3 suggests that Li$^+$ is displacing the Mg^{2+} ions, because Li$^+$ contains only two electrons, which would be undetectable at this resolution. However, the presence of positive $F_o - F_c$ difference density at metal site 2 suggests a deficiency of electrons in the refined model. We therefore modeled a Li$^+$ ion at metal site 2 (Figure 4B). Subsequent refinement of the structure with Li$^+$ occupying metal site 2 resulted in a disappearance of the $F_o - F_c$ difference density but no appearance of $2F_o - F_c$ electron density. Placement of any other metal (Na$^+$, K$^+$, Mg^{2+}, or Zn^{2+}) or water at this site resulted in significant negative $F_o - F_c$ difference density, suggesting too many electrons in the refined model.

This Li$^+$ at metal site 2 is tetrahedrally coordinated by three aspartate side chains from the enzyme (Asp91, Asp94, and Asp212) and the phosphate oxygen of the 3′-phosphate from the PAP molecule (Figure 4B). The average coordination distance between the Li$^+$ and the four oxygen ligands is 1.95 Å, a distance too short for ideal Na$^+$ or K$^+$ geometry.[57] Searching the Cambridge Structural Database (www.ccdc.cam.ac.uk/products/csd) reveals that the most common coordination for Li$^+$ ions is tetrahedral geometry with an average oxygen ligand distance of 1.95 Å. Therefore, we propose that Li$^+$ binds to metal site 2 with tetrahedral coordination.

The occupation of metal site 2 by lithium may inhibit enzyme activity because Li$^+$ prefers tetrahedral coordination as observed in the substrate-bound PAP structure, while Mg^{2+} prefers octahedral coordination only obtained in the product-bound state (AMP and P$_i$). In the PAP structure, a water molecule is nearby that hydrogen bonds to the indole nitrogen of Trp211 but is 3.6 Å from the Li$^+$ ion. This water will move upon binding of Mg^{2+} to metal site 2, where it serves as a ligand for Mg^{2+} (see below). Upon hydrolysis, the 3′-OH of AMP then becomes the final ligand for Mg^{2+} ion in site 2.

The yeast Hal2p protein was also crystallized with PAP in the presence of lithium.[39] However, the determined structure revealed the enzyme hydrolyzed the substrate because products AMP and P$_i$ were observed in the active site, along with metal sites 1 and 3 occupied by Mg^{2+}.[39] The authors deduced that Li$^+$ resides in metal site 2. The Hal2p enzyme may have displayed some activity during the crystallization process, resulting in the product-bound structure, because the enzyme was crystallized in a relatively low concentration of Li$^+$ (5 mM), while the structure reported here was crystallized in 200 mM Li$^+$.

AMP and P$_i$ Structures. Two different structures were determined with bound products, AMP and P$_i$, and Mg^{2+} ions, from two different crystals. Both structures revealed AMP and phosphate binding; however, one structure contained two Mg^{2+} ions bound to metal sites 1 and 2 (not shown), while the other structure contained three Mg^{2+} ions (Figure 4C). These structures correlate well with metal site 3 having the lowest affinity. All three Mg^{2+} ions are octahedrally coordinated.

The Mg^{2+} bound to metal site 1 has all the same ligands as seen in the inhibited PAP structure, except the water molecule ligand that likely serves as the nucleophile is absent and replaced with a phosphate oxygen of the product (Figure 4C). This phosphate oxygen is within hydrogen bonding distance of Thr96 and likely represents the same oxygen of the nucleophile after catalysis.

Metal site 2 is occupied by a Mg^{2+} ion and is octahedrally coordinated by six oxygen atoms. Four of the ligands are the same ligands that coordinate the putative Li$^+$ ion in the inhibited PAP-bound structure. The fifth ligand comes from the 3′-OH of the AMP ribose, which becomes available only after catalysis. The sixth ligand is a water molecule, which also hydrogen bonds to the indole nitrogen of the strictly conserved Trp211 (Figure 4C), which is also observed in the yeast Hal2p structure.[44] Trp211 makes van der Waals contacts against the aliphatic portion of Glu73. Therefore, conserved Trp211 is indirectly involved in binding all three Mg^{2+} ions by positioning Glu73, which coordinates Mg^{2+} ions at site 1 and 3, and tethering the water ligand for metal site 2.

The final metal site 3 is also occupied by a Mg^{2+} ion and coordinated by the Oε2 atom of Glu73, a phosphate oxygen, and four water ligands (Figure 4C). Coordination by four water molecules helps explain its binding affinity being the lowest compared to those of the other metal sites. Thus, the phosphate product is involved in coordinating all three metal sites; one oxygen atom bridges sites 1 and 2, while a different phosphate oxygen ligates metal 3. All the side chains that ligate the three metals are strictly conserved (Asp91, Aps94, Glu73, and Asp212) (Figure 5). Both carboxylate oxygens in Asp91 and Glu73 serve as ligands to two different metals in a bifurcated interaction; Asp91 ligates Mg^{2+} at site 1 and Mg^{2+} at site 2, while Glu73 ligates Mg^{2+} at site 1 and Mg^{2+} at site 3 (Figure 4C).

The adenosine 5′-nucleotide makes very few contacts with the enzyme in both the AMP- and PAP-bound structures. Adenine makes only one hydrogen bond to the enzyme, N^6 hydrogen bonds to the main chain carbonyl oxygen of Gly206 (Figure 4B). The ribose makes no contacts with the enzyme. All three terminal phosphate oxygen atoms of the 5′-phosphate make an interaction with the enzyme. One forms an ionic bond to the conserved Lys190 side chain amine. The side chain of Ser162 hydrogen bonds to the second 5′-phosphate oxygen. While serine is frequently seen in this position, it is not conserved. The third nonbridging phosphate oxygen hydrogen bonds to the main chain amide nitrogen of Ser186. These few contacts between the enzyme and the substrate may help explain the promiscuity of the enzyme to other saccharide phosphate substrates like IMP and FBP.[31]

Phosphate-Bound Structures. Two structures were determined that contained only phosphate and metal ions, one with Ca^{2+} and the other with Mg^{2+}. In both structures, the metal ions reside in sites 1 and 2 (not shown). The phosphate binds in the same position and orientation as the phosphate observed in the AMP and P$_i$ product-bound structure. Like the AMP and P$_i$ structure, one phosphate oxygen bridges both metals. All other
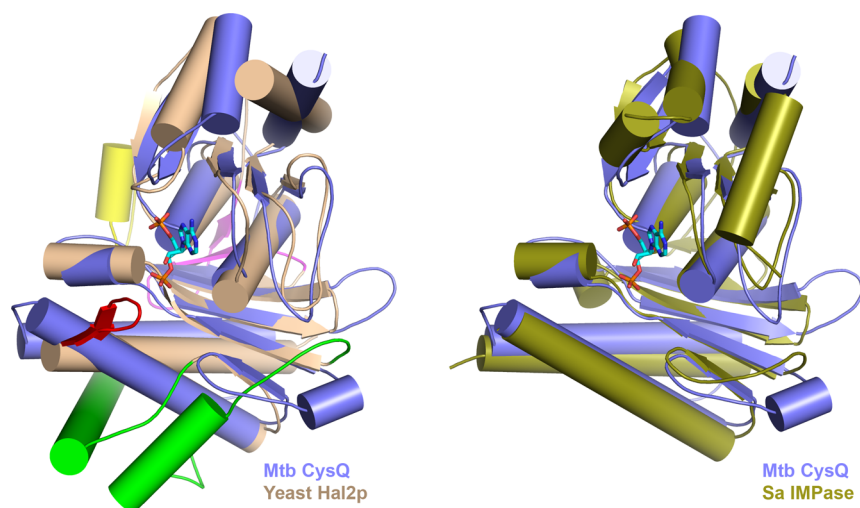
Figure 6. Superposition of *Mtb* CysQ (slate blue) onto yeast (A) yeast Hal2p (sand) and (B) *S. aureus* IMPase (olive green). The *Mtb* CysQ structure superimposes with an rmsd of 2.07 Å onto yeast Hal2p (16.9% identical) and 1.96 Å onto *S. aureus* IMPase (19.2% identical). The yeast Hal2p structure contains four large inserts not in *Mtb* CysQ, which are colored red, green, yellow, and magenta. PAP as seen in *Mtb* CysQ is shown as sticks to mark the active site.
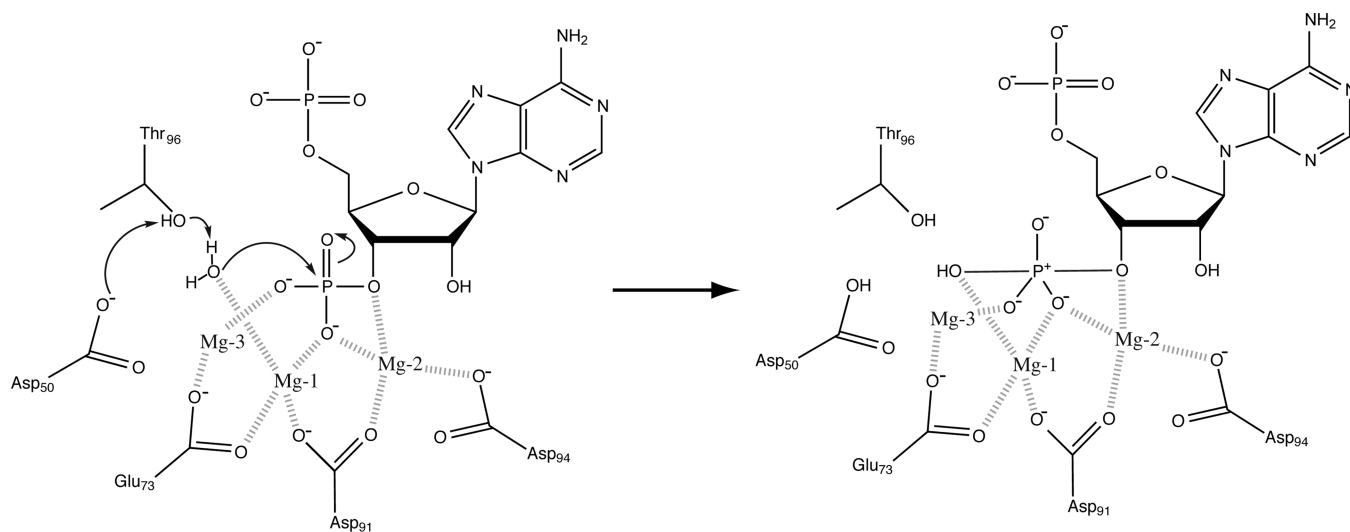
Figure 7. Proposed mechanism for CysQ. The left panel represents the Michaelis–Menten complex as compiled by the *Mtb* CysQ PAP-bound and AMP-, P_i-, and $3Mg^{2+}$-bound structures. The red arrows represent electron movement. Asp50 deprotonates Thr96 that deprotonates the water (ligating Mg-1), which attacks the phosphate. The right panel represents the pentacovalent 3′-phosphate transition state, which is stabilized by the three Mg^{2+} ions. Not all Mg^{2+} ligands are shown for the sake of clarity.

metal coordinate ligands are identical, as well, with the exception of metal site 2, where water replaces the vacated 3′-OH ligand because of the absence of a nucleotide. Additionally, because there is no nucleotide bound, the $\beta6-\alpha4$ loop, along with Arg165, remains in the up position similar to the ligand-free structure (Figure 3).

Comparison to Other Structures. *Mtb* CysQ and yeast CysQ (Hal2p) are 16.9% identical in sequence (37.9% similar) (Figure 5) and superimpose with an rmsd of 2.07 Å over 226 equivalent α-carbons (Figure 6). Analyzing the superposition reveals that the yeast structure has four significant sequence and structural inserts compared to *Mtb* CysQ. The first insert is a short β-hairpin at the start of helix α2 (red in Figure 6). This β-hairpin is near catalytic residues Asp50 and Thr96 and may influence their disposition. This β-hairpin, which is absent in *Mtb* CysQ, is also observed in many other CysQ, IMPase, and FBPase structures.

Another major insert occurs after $\beta1$. In *Mtb* CysQ, the $\beta1-\beta2$ loop is short and contains a single-turn 3_{10}-helix. In Hal2p, a large insert (58 residues) forms two additional long helices (green in Figure 6) that pack up against helices α1 and α2. Similarly, this insert is seen in other CysQ structures, including *E. histolytica*. The third and fourth inserts in Hal2p (compared to *Mtb* CysQ) flank $\beta5$. In *Mtb* CysQ, the loop between $\beta4$ and $\beta5$ is five residues long; in Hal2p, it is 20 residues long and includes a short α-helix (yellow in Figure 6). The insert after $\beta5$ in Hal2p actually augments the β-sheet by adding two additional β-strands with a β-meander topology (magenta in Figure 6) before proceeding up to the C-terminal domain β-sheet. These inserts are also found in *Entamoeba* CysQ and human CysQ (Figure 5). The functional relationship of the absence of these inserts for *Mtb* CysQ is unknown.

The closest homologue of known structure to *Mtb* CysQ is an IMPase from *S. aureus* (PDB entry 3T0J), which is 19.2%

identical in primary sequence (Figure 5). Superposition of this structure onto *Mtb* CysQ (rmsd of 1.96 Å) reveals it does not contain the insets as found in other CysQs from yeast, human, and *Entamoeba* (Figures 5 and 6B). However, *S. aureus* IMPase does contain an extra β-strand after β5 (Figures 5 and 6B).

Mechanism. The CysQ subfamily has a highly conserved metal binding loop consisting of 91-DP(L/I)DGT-96, where Asp91 and Asp94 of this loop together with conserved Glu73, Glu74, Trp211, and Asp212 coordinate the three Mg^{2+} ions. (Figures 4 and 5). Additionally, Asp50 is strictly conserved and is within hydrogen bonding distance of Thr96 Oγ1, which in turn hydrogen bonds to the water that serves as the nucleophile (Figure 4B). This water should have a depressed pK_a because of its ligation to Mg^{2+} at metal site 2.[58,59] Therefore, it will likely be deprotonated by Thr96, which is deprotonated by Asp50. Thus, Asp50 serves as a general base that activates Thr96, which in turn deprotonates the water ligand. The three Mg^{2+} ions will stabilize the pentacovalent transition state of the 3′-phosphate as the hydroxide attacks the phosphorus atom (Figure 7). The leaving group would be the 3′-oxygen of the ribose, which because of its surface exposure, can likely be protonated from bulk solvent.

The specificity of a 5′-phosphate or bis-phosphate sugars for CysQ, IPPases, and FBPases can likely come from a conserved positively charged residue, Lys190 in CysQ, that ion pairs with the nonhydrolyzed phosphate. In CysQ and IPPases, this residue is mostly lysine, while in FBPase, it is mostly arginine. In the IMPases, which catalyze hydrolysis of the phospho group of *myo*-inositol 1-phosphate, this positively charged residue is not conserved (Figure 5). In fact, it is a negatively charged residue for many IMPases, which would block inositol bis-phosphates from binding.

Finally, there has been a report that *Mtb* CysQ displays some phosphatase activity toward PAPS, generating APS and P_i.[31] The structures of *Mtb* CysQ reported here show that the 5′-phosphate is partially solvent exposed (Figure 4) and can therefore accommodate the sulfate group bonded to the 5′-phosphate.

Approximately 3.5% of all new cases of TB display multidrug resistance to drugs used for the past 40−60 years. A new class of inhibitors is needed to treat the growing threat of multidrug-resistant TB. The sulfur activation pathway is implicated as one such pathway for novel drug development. The CysQ structures reported here provide the first structural glimpses of enzymes in this pathway of *M. tuberculosis*. Taken together, the six structures of *Mtb* CysQ reported here give a better perspective on the substrate specificity and catalytic mechanism of this important enzyme. Future studies can use these structures to facilitate rational inhibitor design and exploit the differences between CysQ and the larger FIG family of phosphatases.

■ **AUTHOR INFORMATION**

Corresponding Author

*Department of Chemistry and Department of Molecular and Cellular Biology, University of California, One Shields Ave., Davis, CA 95616. E-mail: ajfisher@ucdavis.edu. Phone: 530-754-6180. Fax: 530-752-8995.

Notes

The authors declare no competing financial interest.

■ **ABBREVIATIONS**

PAP, phosphoadenosine 5′-phosphate; APS, adenosine 5′-phosphosulfate; PAPS, 3′-phosphoadenosine 5′-phosphosulfate; AMP, adenosine monophosphate; TB, tuberculosis; *Mtb*, *M. tuberculosis*; MDR-TB, multidrug-resistant TB; XDR-TB, extensive drug-resistant TB.

■ **REFERENCES**

(1) Global tuberculosis report 2014 (2014) World Health Organization, Geneva.

(2) Fauci, A. S., and Group, N. T. W. (2008) Multidrug-resistant and extensively drug-resistant tuberculosis: the National Institute of Allergy and Infectious Diseases Research agenda and recommendations for priority research. *J. Infect. Dis.* 197, 1493−1498.

(3) Hatzios, S. K., and Bertozzi, C. R. (2011) The regulation of sulfur metabolism in Mycobacterium tuberculosis. *PLoS Pathog.* 7, e1002036.

(4) Pinto, R., Leotta, L., Shanahan, E. R., West, N. P., Leyh, T. S., Britton, W., and Triccas, J. A. (2013) Host cell-induced components of the sulfate assimilation pathway are major protective antigens of Mycobacterium tuberculosis. *J. Infect. Dis.* 207, 778−785.

(5) Schelle, M. W., and Bertozzi, C. R. (2006) Sulfate metabolism in mycobacteria. *ChemBioChem* 7, 1516−1524.

(6) Hampshire, T., Soneji, S., Bacon, J., James, B. W., Hinds, J., Laing, K., Stabler, R. A., Marsh, P. D., and Butcher, P. D. (2004) Stationary phase gene expression of Mycobacterium tuberculosis following a progressive nutrient depletion: a model for persistent organisms? *Tuberculosis (Oxford, U. K.)* 84, 228−238.

(7) Manganelli, R., Voskuil, M. I., Schoolnik, G. K., Dubnau, E., Gomez, M., and Smith, I. (2002) Role of the extracytoplasmic-function sigma factor sigma(H) in Mycobacterium tuberculosis global gene expression. *Mol. Microbiol.* 45, 365−374.

(8) Pinto, R., Tang, Q. X., Britton, W. J., Leyh, T. S., and Triccas, J. A. (2004) The Mycobacterium tuberculosis cysD and cysNC genes form a stress-induced operon that encodes a tri-functional sulfate-activating complex. *Microbiology* 150, 1681−1686.

(9) Rengarajan, J., Bloom, B. R., and Rubin, E. J. (2005) Genome-wide requirements for Mycobacterium tuberculosis adaptation and survival in macrophages. *Proc. Natl. Acad. Sci. U. S. A.* 102, 8327−8332.

(10) Sassetti, C., Boyd, D., and Rubin, E. (2001) Comprehensive identification of conditionally essential genes in mycobacteria. *Proc. Natl. Acad. Sci. U. S. A.* 98, 12712−12717.

(11) Bhave, D. P., Muse, W. B., 3rd, and Carroll, K. S. (2007) Drug targets in mycobacterial sulfur metabolism. *Infect. Disord.: Drug Targets* 7, 140−158.

(12) Paritala, H., and Carroll, K. S. (2013) New targets and inhibitors of mycobacterial sulfur metabolism. *Infect. Disord.: Drug Targets* 13, 85−115.

(13) Zeng, L., Shi, T., Zhao, Q., and Xie, J. (2013) Mycobacterium sulfur metabolism and implications for novel drug targets. *Cell Biochem. Biophys.* 65, 77−83.

(14) Sekowska, A., Kung, H.-F., and Danchin, A. (2000) Sulfur Metabolism in Escherichia coli and Related Bacteria: Facts and Fiction. *J. Mol. Microbiol. Biotechnol.* 2, 34.

(15) Segel, I. H., Renosto, F., and Seubert, P. A. (1987) Sulfate-activating enzymes. *Methods Enzymol. 143*, 334−349.

(16) Mougous, J. D., Green, R. E., Williams, S. J., Brenner, S. E., and Bertozzi, C. R. (2002) Sulfotransferases and sulfatases in mycobacteria. *Chem. Biol. 9*, 767−776.

(17) Monigatti, F., Hekking, B., and Steen, H. (2006) Protein sulfation analysis–A primer. *Biochim. Biophys. Acta, Proteins Proteomics 1764*, 1904−1913.

(18) Pi, N., Hoang, M. B., Gao, H., Mougous, J. D., Bertozzi, C. R., and Leary, J. A. (2005) Kinetic measurements and mechanism determination of Stf0 sulfotransferase using mass spectrometry. *Anal. Biochem. 341*, 94−104.

(19) Hatzios, S. K., Schelle, M. W., Newton, G. L., Sogi, K. M., Holsclaw, C. M., Fahey, R. C., and Bertozzi, C. R. (2011) The Mycobacterium tuberculosis CysQ phosphatase modulates the biosynthesis of sulfated glycolipids and bacterial growth. *Bioorg. Med. Chem. Lett. 21*, 4956−4959.

(20) Neuwald, A. F., Krishnan, B. R., Brikun, I., Kulakauskas, S., Suziedelis, K., Tomcsanyi, T., Leyh, T. S., and Berg, D. E. (1992) cysQ, a gene needed for cysteine synthesis in Escherichia coli K-12 only during aerobic growth. *J. Bacteriol. 174*, 415−425.

(21) Murguia, J. R., Belles, J. M., and Serrano, R. (1995) A salt-sensitive 3′(2′),5′-bisphosphate nucleotidase involved in sulfate activation. *Science 267*, 232−234.

(22) Roth, J. A., Rivett, A. J., and Renskers, K. J. (1982) Properties of human brain phenol sulfotransferase and its role in the activation of catecholamine neurotransmitters. In *Sulfate Metabolism and Sulfate Conjugation* (Mulder, G. J., Caldwell, J., Van Kempen, G. M. J., and Vonk, R. J., Eds.) pp 107−114, Taylor and Francis, London.

(23) Dichtl, B., Stevens, A., and Tollervey, D. (1997) Lithium toxicity in yeast is due to the inhibition of RNA processing enzymes. *EMBO J. 16*, 7184−7195.

(24) Carroll, K., Gao, H., Chen, H., Stout, C., Leary, J., and Bertozzi, C. (2005) A Conserved Mechanism for Sulfonucleotide Reduction. *PLoS Biol. 3*, e250.

(25) Gu, X., Chen, M., Shen, H., Jiang, X., Huang, Y., and Wang, H. (2006) Rv2131c gene product: an unconventional enzyme that is both inositol monophosphatase and fructose-1,6-bisphosphatase. *Biochem. Biophys. Res. Commun. 339*, 897−904.

(26) Quintero, F. J., Garciadeblas, B., and Rodriguez-Navarro, A. (1996) The SAL1 gene of Arabidopsis, encoding an enzyme with 3′(2′),5′-bisphosphate nucleotidase and inositol polyphosphate 1-phosphatase activities, increases salt tolerance in yeast. *Plant Cell 8*, 529−537.

(27) Faisal Tarique, K., Arif Abdul Rehman, S., and Gourinath, S. (2014) Structural elucidation of a dual-activity PAP phosphatase-1 from Entamoeba histolytica capable of hydrolysing both 3′-phosphoadenosine 5′-phosphate and inositol 1,4-bisphosphate. *Acta Crystallogr., Sect. D: Biol. Crystallogr. 70*, 2019−2031.

(28) Fukuda, C., Kawai, S., and Murata, K. (2007) NADP(H) phosphatase activities of archaeal inositol monophosphatase and eubacterial 3′-phosphoadenosine 5′-phosphate phosphatase. *Appl. Environ. Microbiol. 73*, 5447−5452.

(29) Johnson, K. A., Chen, L., Yang, H., Roberts, M. F., and Stec, B. (2001) Crystal structure and catalytic mechanism of the MJ0109 gene product: a bifunctional enzyme with inositol monophosphatase and fructose 1,6-bisphosphatase activities. *Biochemistry 40*, 618−630.

(30) Stec, B., Yang, H., Johnson, K. A., Chen, L., and Roberts, M. F. (2000) MJ0109 is an enzyme that is both an inositol monophosphatase and the 'missing' archaeal fructose-1,6-bisphosphatase. *Nat. Struct. Biol. 7*, 1046−1050.

(31) Hatzios, S. K., Iavarone, A. T., and Bertozzi, C. R. (2008) Rv2131c from Mycobacterium tuberculosis is a CysQ 3′-phosphoadenosine-5′-phosphatase. *Biochemistry 47*, 5823−5831.

(32) Majerus, P. W. (1992) Inositol phosphate biochemistry. *Annu. Rev. Biochem. 61*, 225−250.

(33) Choe, J. Y., Poland, B. W., Fromm, H. J., and Honzatko, R. B. (1998) Role of a dynamic loop in cation activation and allosteric regulation of recombinant porcine fructose-1,6-bisphosphatase. *Biochemistry 37*, 11441−11450.

(34) Gill, R., Mohammed, F., Badyal, R., Coates, L., Erskine, P., Thompson, D., Cooper, J., Gore, M., and Wood, S. (2005) High-resolution structure of myo-inositol monophosphatase, the putative target of lithium therapy. *Acta Crystallogr., Sect. D: Biol. Crystallogr. 61*, 545−555.

(35) Strasser, F., Pelton, P. D., and Ganzhorn, A. J. (1995) Kinetic characterization of enzyme forms involved in metal ion activation and inhibition of myo-inositol monophosphatase. *Biochem. J. 307* (Part 2), 585−593.

(36) York, J. D., Ponder, J. W., and Majerus, P. W. (1995) Definition of a metal-dependent/Li(+)-inhibited phosphomonoesterase protein family based upon a conserved three-dimensional core structure. *Proc. Natl. Acad. Sci. U. S. A. 92*, 5149−5153.

(37) Leech, A. P., Baker, G. R., Shute, J. K., Cohen, M. A., and Gani, D. (1993) Chemical and kinetic mechanism of the inositol mono-phosphatase reaction and its inhibition by Li+. *Eur. J. Biochem. 212*, 693−704.

(38) Dudev, T., and Lim, C. (2011) Competition between Li+ and Mg2+ in metalloproteins. Implications for lithium therapy. *J. Am. Chem. Soc. 133*, 9506−9515.

(39) Albert, A., Yenush, L., Gil-Mascarell, M. R., Rodriguez, P. L., Patel, S., Martinez-Ripoll, M., Blundell, T. L., and Serrano, R. (2000) X-ray structure of yeast Hal2p, a major target of lithium and sodium toxicity, and identification of framework interactions determining cation sensitivity. *J. Mol. Biol. 295*, 927−938.

(40) Berridge, M. J., Downes, C. P., and Hanley, M. R. (1989) Neural and developmental actions of lithium: a unifying hypothesis. *Cell 59*, 411−419.

(41) Brown, K. M., and Tracy, D. K. (2013) Lithium: the pharmacodynamic actions of the amazing ion. *Ther. Adv. Psychopharmacol. 3*, 163−176.

(42) Miller, D. J., and Allemann, R. K. (2007) myo-Inositol monophosphatase: a challenging target for mood stabilising drugs. *Mini-Rev. Med. Chem. 7*, 107−113.

(43) Nahorski, S. R., Ragan, C. I., and Challiss, R. A. (1991) Lithium and the phosphoinositide cycle: an example of uncompetitive inhibition and its pharmacological consequences. *Trends Pharmacol. Sci. 12*, 297−303.

(44) Patel, S., Martinez-Ripoll, M., Blundell, T. L., and Albert, A. (2002) Structural enzymology of Li(+)-sensitive/Mg(2+)-dependent phosphatases. *J. Mol. Biol. 320*, 1087−1094.

(45) Erickson, A. I., Sarsam, R. D., and Fisher, A. J. (2014) Expression, purification and preliminary crystallographic analysis of Mycobacterium tuberculosis CysQ, a phosphatase involved in sulfur metabolism. *Acta Crystallogr., Sect. F: Struct. Biol. Commun. 70*, 750−753.

(46) Kabsch, W. (2010) XDS. *Acta Crystallogr., Sect. D: Biol. Crystallogr. 66*, 125−132.

(47) Kabsch, W. (2010) Integration, scaling, space-group assignment and post-refinement. *Acta Crystallogr., Sect. D: Biol. Crystallogr. 66*, 133−144.

(48) Matthews, B. W. (1968) Solvent content of protein crystals. *J. Mol. Biol. 33*, 491−497.

(49) Sheldrick, G. M. (2010) Experimental phasing with SHELXC/D/E: combining chain tracing with density modification. *Acta Crystallogr., Sect. D: Biol. Crystallogr. 66*, 479−485.

(50) Adams, P. D., Afonine, P. V., Bunkoczi, G., Chen, V. B., Davis, I. W., Echols, N., Headd, J. J., Hung, L. W., Kapral, G. J., Grosse-Kunstleve, R. W., McCoy, A. J., Moriarty, N. W., Oeffner, R., Read, R. J., Richardson, D. C., Richardson, J. S., Terwilliger, T. C., and Zwart, P. H. (2010) PHENIX: a comprehensive Python-based system for macromolecular structure solution. *Acta Crystallogr., Sect. D: Biol. Crystallogr. 66*, 213−221.

(51) Emsley, P., and Cowtan, K. (2004) Coot: model-building tools for molecular graphics. *Acta Crystallogr., Sect. D: Biol. Crystallogr. 60*, 2126−2132.

(52) McCoy, A. (2007) Solving structures of protein complexes by molecular replacement with Phaser. *Acta Crystallogr., Sect. D: Biol. Crystallogr. 63*, 32−41.

(53) Collaborative Computational Project Number 4 (1994) The CCP4 suite: Programs for protein crystallography. *Acta Crystallogr., Sect. D: Biol. Crystallogr. 50*, 760−763.

(54) Stieglitz, K. A., Roberts, M. F., Li, W., and Stec, B. (2007) Crystal structure of the tetrameric inositol 1-phosphate phosphatase (TM1415) from the hyperthermophile, Thermotoga maritima. *FEBS J. 274*, 2461−2469.

(55) Bone, R., Frank, L., Springer, J. P., and Atack, J. R. (1994) Structural studies of metal binding by inositol monophosphatase: evidence for two-metal ion catalysis. *Biochemistry 33*, 9468−9476.

(56) Pollack, S. J., Atack, J. R., Knowles, M. R., McAllister, G., Ragan, C. I., Baker, R., Fletcher, S. R., Iversen, L. L., and Broughton, H. B. (1994) Mechanism of inositol monophosphatase, the putative target of lithium therapy. *Proc. Natl. Acad. Sci. U. S. A. 91*, 5766−5770.

(57) Andreini, C., Cavallaro, G., Lorenzini, S., and Rosato, A. (2013) MetalPDB: a database of metal sites in biological macromolecular structures. *Nucleic Acids Res. 41*, D312−319.

(58) Burgess, J. (1988) *Ions in solution: Basic principles of chemical interactions* (Horwood, E., Ed.) Halsted Press, Chichester, England.

(59) Chin, J., and Kim, H. J. (2005) Artificial Hydrolytic Metalloenzymes. In *Artificial Enzymes* (Breslow, R., Ed.) pp 133−157.

(60) Chen, V. B., Arendall, W. B., 3rd, Headd, J. J., Keedy, D. A., Immormino, R. M., Kapral, G. J., Murray, L. W., Richardson, J. S., and Richardson, D. C. (2010) MolProbity: all-atom structure validation for macromolecular crystallography. *Acta Crystallogr., Sect. D: Biol. Crystallogr. 66*, 12−21.

(61) Robert, X., and Gouet, P. (2014) Deciphering key features in protein structures with the new ENDscript server. *Nucleic Acids Res. 42*, W320−324.